Co-Evaporation of Doped Inorganic Carrier Selective Layers for High-Performance Inverted Planar Perovskite Solar Cells

Jiexuan Jiang,[1] Andraž Mavrič,[2] Nadiia Pastukhova,[1,2] Matjaz Valant,[2] Qiugui Zeng,[1] Zeyu Fan,[1] Beibei Zhang,[1] and Yanbo Li[1,]*

[1]Institute of Fundamental and Frontier Sciences, University of Electronic Science and Technology of China, Chengdu 610054, China

[2]University of Nova Gorica, Materials Research Laboratory, Vipavska 13, SI-5000 Nova Gorica, Slovenia

[*]Corresponding author: yanboli@uestc.edu.cn

Keywords: Carrier selective layers, Cu-doped nickel oxide, W-doped niobium oxide, perovskite solar cells, electron-beam evaporation.

This article has been accepted for publication and undergone full peer review but has not been through the copyediting, typesetting, pagination and proofreading process, which may lead to differences between this version and the Version of Record. Please cite this article as doi: 10.1002/solr.202200091.

Abstract

Inorganic carrier selective layers (CSLs), whose conductivity can be effectively tuned by doping, offer low-cost and stable alternatives for their organic counterparts in perovskite solar cells (PSCs). Herein, we employ a dual-source electron-beam co-evaporation method for the controlled deposition of copper-doped nickel oxide (Cu:NiO) and tungsten-doped niobium oxide ($W:Nb_2O_5$) as hole and electron transport layers, respectively. The mechanisms for the improved conductivity using dopants are investigated. Owing to the improved conductivity and optimized band alignment of the doped CSLs, the all-inorganic-CSLs-based PSCs achieves a maximum power conversion efficiency (PCE) of 20.47%. Furthermore, a thin titanium buffer layer is inserted between the $W:Nb_2O_5$ and the silver electrode to prevent the halide ingression and improve band alignment. This leads to a further improvement of PCE to 21.32% and a long-term stability (1200 h) after encapsulation. Finally, the large-scale applicability of the doped CSLs by co-evaporation is demonstrated for the device with 1 cm^2 area showing a PCE of over 19%. Our results demonstrate the potential application of the co-evaporated CSLs with controlled doping in PSCs for commercialization.

Introduction

Perovskite solar cell (PSC) is a promising candidate in emerging photovoltaic technologies because it offers high power conversion efficiency (PCE) via simple and cost-effective fabrication routes. PSC has already attained a maximum PCE of 25.6%, comparable to other commercialized photovoltaic technologies (e.g., c-Si and CdTe).[1-5] One important research trend is to further improve PSC's operational stability and cost-effectiveness through the integration of low-cost inorganic carrier selective layers (CSLs).[6-8] Inorganic CSLs are attractive mainly because they are more stable, less expensive, and allow for large-scale fabrication compared with organic CSLs.[9-11] Titanium oxide (TiO_2),[12, 13] niobium oxide (Nb_2O_5),[14] and tin oxide (SnO_2) are some of the commonly utilized electron transport layers (ETL), while nickel oxide (NiO), vanadium oxide (V_2O_5), and cuprous thiocyanate (CuSCN) are widely employed as hole transport layers (HTLs),[15-17] The utilization of these air-stable inorganic CSLs can improve the operational stability of PSCs, as organic CSLs easily degrade while exposed to humidity, e.g. [6,6]-phenyl C61 butyric acid methyl ester (PCBM) and 2,2',7,7'-tetrakis (N, N-i-4-methoxyphenylamino)-9,9-spirobifluorene(spiro-MeOTAD).[18,19] In most cases, the inorganic CSLs are used in combination with organic counterparts to fabricate conventional n(inorganic)-i-p(organic) or p(inorganic)-i-n(organic) type PSCs. The stability of these PSCs is still largely limited by the organic CSLs. Recently, PSCs with all-inorganic ETL and HTL have been reported to show much improved operational stability. Han *et al.* reported an inorganic CSL-based PSC composed as FTO/NiMgLiO/perovskite/PCBM/Ti(Nb)O_x/Ag. Although organic PCBM was used, the addition of an inorganic Ti(Nb)O_x interlayer allowed the device to maintain 90% of its initial efficiency after 1000-h of continuous operation.[20] Yang et al. first demonstrated an organic CSL-free PSC composed as ITO/NiO_x/perovskite/ZnO/Al with PCE of 16.1% and 90% of the

initial PCE was maintained after storing the device in ambient air for 60 days.[21] Grätzel et al. reported a FTO/TiO_2/perovskite/CuSCN/rGO/Au device with PCE over 20% and >95% of its initial efficiency after aging for 1000 hours under full-sun illumination at 60°C. [22] These results demonstrated that efficient and stable PSCs could be achieved with inorganic CSLs, creating an opportunity for practical applications.[23]

Recently, our group reported a ITO/NiO/perovskite/Nb_2O_5/Ag device architecture that achieved a maximum PCE of over 19% using electron-beam (EB) deposited inorganic CSLs.[24,25] The EB-evaporated NiO HTL and Nb_2O_5 ETL exhibit high charge extraction efficiencies and effective charge blocking capabilities, resulting in high photovoltage for the inverted p-i-n planar PSC. It is widely known that doping of metal oxides with proper cations could improve their electrical conductivity and adjust their energy band positions,[26,27] which could further improve charge extraction efficiency of the inorganic CSLs. Various metal cations (e.g., Cu^{2+}, Li^{+}, Mg^{2+}, Co^{2+}, Zn^{2+}) have been employed for doping NiO HTL.[28,29] Among them, Cu-doped NiO (Cu:NiO) is the most widely used and usually synthesized by solution processes.[30-32] However, an effective doping strategy for Nb_2O_5 ETL has not been reported because it is relatively novel to PSC devics, although there are a few reports on doped-Nb_2O_5 nanoparticles or thin films for other applications.[33-34] Proper doping of Nb_2O_5 is expected to further improve the eccicency of this type of all-inorganic CSL-based PSC.[35] Herein, we employ dual-source EB co-evaporation for controlled deposition of Cu:NiO HTL and tungsten doped-Nb_2O_5 (W:Nb_2O_5) ETL. The doped inorganic CSLs exhibit higher electrical conductivity and improved energy level alignment, resulting in an enhanced carrier extraction efficiency of the PSC. Furthermore, a thin Ti buffer layer was employed to modify the interface between the W:Nb_2O_5 ETL and the Ag counter electrode.[36] The Ti buffer layer not only enhanced the efficiency of the PSC by smoothing carrier collection at

the counter electrode, but also improved the stability of the PSC by preventing the migration of halide ions to react with the Ag electrode. As a result, the ITO/Cu:NiO/perovskite/W:Nb_2O_5/Ti/Ag device achieved a maximum PCE of 21.32% and maintained 98% of its initial PCE after 1200 h with encapsulation. The compatibility of the EB co-evaporation process for large-scale device fabrication was also demonstrated by preparing a 1-cm^2 device yielding a PCE of over 19%. These results demonstrate that the doped inorganic CSLs deposited by EB co-evaporation have potential to be used in PSCs for practical applications.

Results and Discussions

Figure 1a shows the schematic drawing for the co-evaporation of inorganic Cu:NiO and W:Nb_2O_5 CSLs using dual-source EB evaporation. **Figure 1b-c** show typical scanning electron microscopy (SEM) images of the EB-deposited Cu:NiO and W:Nb_2O_5 films. The doping concentration of Cu in NiO HTL was first optimized in a PSC device consisted of ITO/Cu:NiO/$FA_{0.85}MA_{0.15}PbI_{2.55}Br_{0.45}$/$Nb_2O_5$/Ag. From the J-V curves in **Figure 1d** and device parameters in **Table 1**, the highest PCE of 19.94% was achieved with a Cu doping concentration of 3% (Cu:Ni atomic ratio estimated from the EB deposition rates) in NiO HTL. Subsequently, the doping concentration of W in Nb_2O_5 ETL was optimized using the 3%-Cu:NiO HTL based PSCs. The J-V curves in **Figure 1e** and device parameters in **Table 2** revealed that the maximum PCE was further increased to 20.47% with a W doping concentration of 2% (W:Nb atomic ratio) in Nb_2O_5 ETL. The 3%-Cu:NiO and 2%-W:Nb_2O_5 CSLs were then used for further characterization and device fabrication in the following study.

Figure S1a-b show the SEM images of the NiO films with and without Cu doping. No obvious change in the morphology of the films was observed after Cu doping. However, the X-ray

diffraction (XRD) results in Figure S2a reveals that Cu-doping induces a preferential film growth along the [111] direction in Cu:NiO film, in contrast to the [002] orientation in pristine NiO film. It has been reported that the conductivity of [111]-oriented NiO film is significantly higher than that of [002]-oriented NiO film.[37]. The high-resolution transmission electron microscopy (HRTEM) of a thin film cross-section was employed to analyze the structure of Cu:NiO film deposited on ITO substrate. As shown in **Figure 2a**, a Cu:NiO layer with a uniform thickness of ~34 nm is coated conformally on the ITO substrate. The HRTEM image in **Figure 2b** reveals that Cu:NiO layer is polycrystalline and the sizes of the crystallites range from several to ten nanometers. A d-spacing of ~0.245 nm was measured from the inset in Figure 2b, which matches well with the NiO (111) lattice plane spacing (0.242 nm). The HRTEM result confirms that the Cu-doping indeed induced a preferential film growth along the [111] direction. The scanning TEM (STEM) image in **Figure 2c** and the corresponding energy-dispersive X-ray spectroscopy (EDS) mapping results in **Figure 2d** show an uniform distribution of Cu in the NiO layer. The STEM-EDS line scans of the constituent elements in **Figure 2e** further reveal that the Ni and Cu signals overlap well with each other. Quantitative STEM-EDS analysis gives a Cu/Ni atomic ratio of ~3.3% (Figure S3), which agrees with the estimation from the EB deposition rates.

The SEM images of Nb_2O_5 and W:Nb_2O_5 films in Figure S1c-d show that there is no obvious morphology change after W doping. The XRD patterns in Figure S2b show that the W:Nb_2O_5 film is still amorphous after doping. The HRTEM image in **Figure 3a** show that the thickness of the W:Nb_2O_5 film is approximately 56 nm. While the lattice fringes of Si substrate are clearly observed from the HRTEM image in **Figure 3b**, no clear lattice fringe is observed in the W:Nb_2O_5 layer. This suggests the W:Nb_2O_5 film is indeed amorphous. The STEM image and corresponding EDS mapping results in **Figure 3c-d** show that the W dopants distributed uniformly in the Nb_2O_5 layer,

which is further verified by the EDS line scan results in **Figure 3e**. Quantitative STEM-EDS analysis reveal that the W/Nb atomic ratio is ~2.1% (Figure S4), which is consistent with that estimated from the EB deposition rates. Furthermore, the SEM images in Figure S5 show that EB-deposited Nb_2O_5 and W:Nb_2O_5 films uniformly cover the perovskite film and the underlying grains of the perovskite are well-preserved.

The chemical states of the Cu and W dopants in NiO and Nb_2O_5 were investigated by X–ray photoelectron spectroscopy (XPS). **Figure 4a–c** present the core-level XPS spectra of Cu 2p, Ni 2p, and O 1s for the pristine NiO and Cu:NiO samples, respectively. The survey spectra and the core-level spectra of C 1s are provided in Figure S6. The Cu 2p core level spectrum in Figure 4a shows that the Cu dopants exist in the form of Cu^{2+} and Cu^{+} in the Cu:NiO film, whereas the lower valence Cu^{+} species could serve as acceptors in NiO. For pristine NiO film the p-type conductivity is attributed to the self-doping of Ni^{3+} acceptors.[38] Figure 4b-c show that there is indeed a high concentration of Ni^{3+} species in the pristine NiO film. A Ni^{3+}/Ni^{2+} ratio of 0.69 is obtained by quantitatively analyzing the O 1s core level spectrum in Figure 4c. Figure 4b-c show that the concentration of Ni^{3+} is further increased with Cu doping, resulting in a Ni^{3+}/Ni^{2+} ratio of 0.80 in the Cu:NiO film. Therefore, Cu doping could improve the p-type conductivity of NiO not only by creating Cu^{+} acceptors but also by increasing the concentration of Ni^{3+} acceptors. **Figure 4d–f** show the core-level XPS spectra of W 4f, Nb 3d, and O 1s for the pristine Nb_2O_5 and W:Nb_2O_5 films, respectively. The survey spectra and the core-level spectra of C 1s are provided in Figure S7. By deconvoluting the W 4f spectra from Nb 4p spectra in Figure 2d, the valence state of W dopant is determined to be W^{6+}, which could act as a donor for Nb_2O_5. The improved conductivity of Cu:NiO and W:Nb_2O_5 films were verified by comparing the out-of-plane conductivity of films with and without doping in Figure S8.

The ultraviolet-visible (UV-vis) transmission spectra in Figure S9 show that the Cu:NiO and W:Nb_2O_5 films maintained the high transmittance in the visible range. Tauc plots of the absorption spectra in Figure S10a-b reveal that Cu:NiO and W:Nb_2O_5 films have optical band gaps of 3.62 and 3.83 eV, respectively. Ultraviolet photoelectron spectroscopy (UPS) was employed to determine the work functions and valence band positions for Cu:NiO and W:Nb_2O_5 films (Figure S10c-f). The energy levels are summarized in the schematic band diagrams in Figures S11. The work functions of the Cu:NiO and W:Nb_2O_5 films are located at -4.66 and -4.19 eV, respectively. The valence band maximum (VBM) and conduction band minimum (CBM) lie at -5.31 and -1.69 eV for Cu:NiO film and -7.85 and -4.02 eV for W:Nb_2O_5 film, respectively. Considering a VBM of -5.50 eV and a CBM of -3.89 eV for the $FA_{0.85}MA_{0.15}PbI_{2.55}Br_{4.55}$ perovskite, the band positions of Cu:NiO and W:Nb_2O_5 would facilitate efficient charge extraction from the perovskite layer. To verify this, PL quenching experiments were carried out by employing steady-state and time-resolved photoluminescence (TRPL).[39,40] **Figure 5a** shows the steady-state PL spectra of the perovskite films deposited on glass, NiO/glass, and Cu:NiO/glass substrates. The XRD patterns and UV-Vis absorption spectra of the perovskite films are shown in Figure S12. The PL intensity was quenched to a large extend for perovskite film deposited on Cu:NiO/glass substrate compared to NiO/glass substrate. This suggests Cu:NiO is more efficient in extracting hole from the perovskite layer than pristine NiO, as confirmed by the TRPL results in **Figure 5b**. By fitting the TRPL decay with a bi-exponential decay model, an average lifetime of 1219 ns was obtained for perovskite film deposited on a glass substrate (Table S1). The average lifetimes were shortened to 186 and 16 ns for perovskite films deposited on NiO and Cu:NiO thin films, respectively, demonstrating Cu:NiO has higher hole extraction efficiency than pristine NiO. Similarly, **Figure 5c-d** reveal lower PL intensity and faster TRPL decay for perovskite film with W:Nb_2O_5 employed as ETL compared to using pure Nb_2O_5 as

ETL. The average lifetime of the photocarriers in the perovskite was deceased from 66 to 47 ns when the Nb_2O_5 ETL was doped with W (Table S2). To exclude the possibility that lower PL intensities and faster TRPL decays using doped CSLs may come from increased interfacial trap densities, space-charge limited current (SCLC) technique was used to study the interfacial trap density at the perovskite/CSLs interfaces. Hole-only devices and electron-only devices, whose architectures are shown in the insets in **Figure 5e-f,** were fabricated for SCLC measurements. The SCLC plots show that the current increases linearly in the low-bias region and a sharp non-linear increase is observed when bias voltage exceeds a kink point, which is defined as the trap-filled limit voltage (V_{TFL}). The trap density (n_t) can be calculated according to the following equation;[41]

$$n_t = \frac{2\varepsilon\varepsilon_0 V_{TFL}}{eL^2} \quad (1)$$

where L is the film's thickness, e is the elementary charge, ε_0 and ε are the vacuum permittivity and relative dielectric constant of perovskite (ε = 28.8), respectively. Figure 4e shows V_{TFL} values for the Cu:NiO- and NiO-based devices are 0.36 and 0.57 V, respectively. Notably, a n_t of 3.18×10^{15} cm^{-3} for the Cu:NiO-based device was obtained, as compared to 5.05×10^{15} cm^{-3} for the NiO-based device. Meanwhile, the V_{TFL} values for the Nb_2O_5- and W:Nb_2O_5-based devices in Figure 4f are 0.66 and 0.22 V, corresponding to n_t values of 5.85×10^{15} and 1.92×10^{15} cm^{-3}, respectively. Combining the UPS, TRPL, and SCLC results, it is concluded that the Cu:NiO and W:Nb_2O_5 indeed facilitate more efficient charge carrier extraction from the perovskite layer due to more favorable band alignment and lower interfacial trap densities.

PSCs with Cu:NiO HTL and W:Nb_2O_5 ETL were further optimized by inserting a thin titanium (Ti) buffer layer between ETL and the Ag counter electrode. It has been reported that the Ag electrode is prone to degrade by halide ingression from the perovskite layer, [42] which affects the long-term stability of the PSCs. The Ti buffer layer is therefore employed to prevent the halide

ingression while mediating the carrier collection at the counter electrode. The thickness of the Ti buffer layer was optimized at 10 nm (Figure S13). The optimized device architecture composed as ITO/Cu:NiO/perovskite/W:Nb_2O_5/Ti/Ag is illustrated in **Figure 6a**. The corresponding SEM image of the device cross-section with optimized PSC is shown in **Figure 6b.** The band alignment of each functional layers is shown in **Figure 6c.** Comparing to the control device with standard architecture of ITO/NiO/perovskite/Nb_2O_5/Ag, the optimized device allows a smoother carrier transportation and collection through the PSC device for both electrons and holes. As a result, the optimized device delivered an improved PCE and reduced hysteresis as shown by the J-V curves in **Figure 6d** and the device parameters in **Table 3**. The statistical distribution of PCEs for 50 individual devices in **Figure 6e** show that the average PCEs (with standard deviation) are 18.7±0.4% and 20.7±0.3% for the control and optimized devices, respectively. The statistical distribution of the other key *J*-V parameters (J_{SC}, V_{OC}, and FF) are shown in Figure S14, which show that all the key parameters are improved in the optimized devices. **Figure 6f** presents external quantum efficiency (EQE) spectra for the control and optimized PSCs. Tauc plots of the EQE spectra in Figure S15 show clear cut-off energy at 1.6 eV, which matches well with the band gap of the perovskite obtained from the PL peak positions (774 nm, corresponding to a band gap of 1.60 eV) in Figure 4a-b. Compared with the control device, the EQEs of the optimized device were enhanced in the wavelength range of 400-750 nm. As a result, the integrated J_{SC} obtained by integrating the EQE spectrum with standard AM 1.5G spectrum (ASTM G173-03) was improved from 21.80 mA/cm^2 for the control device to 22.93 mA/cm^2 for the optimized device. The integrated J_{SC} values also agree within 5% of the values measured from the J-V curves (Table 3).

Electrochemical impedance spectroscopy (EIS) was conducted to study carrier recombination kinetics in the PSCs. **Figure 6g** shows the Nyquist plots for the control and optimized devices,

which were fitted using the equivalent circuit model comprised of the series resistance (R_s), the recombination resistance (R_{rec}) and capacitance (C_{rec}), as depicted in the inset of Figure 6g. The fitted parameters from the Nyquist plots are summarized in Table S4. The R_s is decreased from 13.32 Ω in the control device to 11.62 Ω the optimized device, which is ascribed to improved conductivity of the doped CSLs. More obvious change is found for R_{rec}, which increased from 314.8 Ω in the control device to 800.8 Ω in the optimized device. The much larger R_{rec} in the optimized device indicates effective suppression of the charge recombination, which could originate from the rapid carrier extraction through the doped CSLs. Meanwhile, the effective lifetimes (τ_n) were extracted as the reciprocals of the frequencies at the peaks of the semicircles in the Cole-Cole plots.[43,44] The τ_n of the optimized device (9.11 μs) is considerably longer than that of the control (5.08 μs). Therefore, the above results confirm that doped CSLs can effectively suppress interfacial carrier recombination, hence improving the overall photovoltaic performance.

Figure S16 plots the steady-state photocurrent output of the devices, which shows that the operational stability of the optimized device is improved over the control device. For long-term shelf-stability test, the devices were encapsulated in a nitrogen-filled glove box and stored in air with 50±10% RH at room temperature and tested periodically for 1200 h. **Figure 6h** reveals the excellent stability of the optimized device with PCE retained 98% of its initial value after being stored in air for 1200 h. In contrast, the control device retained only 82% of its initial PCE value after the same stability test. The improved stability of the device is attributed to the presence of the Ti interlayer, which not only prohibits inward diffusion of ions from the Ag to the perovskite, but also blocks the outward diffusion of I^- ions onto the electrode. We adopted XRD characterizations to investigate the changes of the electrodes before and after aging the devices at 85 °C for 72 h in N_2 atmosphere. XRD patterns in Figure S17 confirm the formation of AgI is prevented in the device

with Ti interlayer, further demonstrating that the improved stability is ascribed to the effect of Ti buffer layer on blocking halide ingression. Finally, to demonstrate the large-scale applicability of the doped CSLs deposited by dual-source EB co-evaporation method, large-scale devices with an active area of 1 cm^2 were fabricated. **Figure 6i** plots the best J-V curves of the large-scale device and the standard device with an active area of 0.155 cm^2). Although the performance of the large-scale device is lower than that of the smaller device (Table 4), it is still able to achieve a relatively high PCE of 19.01%.

Conclusions

In summary, we proposed a novel EB co-evaporation strategy to prepare Cu:NiO HTL and W:Nb_2O_5 ETL for the fabrication of all-inorganic CSL-based PSCs. The Cu and W doping not only enhanced the conductivity of the CSLs, but also improved the band alignment of the perovskite/CSL heterojunctions, thus improving the overall performance of the all-inorganic CSL-based PSCs. Furthermore, a Ti buffer layer was inserted into the W:Nb_2O_5/Ag interface to improve the device stability by preventing halide ingression to the Ag electrode while mediating a smooth carrier collection at the counter electrode. The optimized ITO/Cu:NiO/perovskite/W:Nb_2O_5/Ti/Ag device yielded a maximum PCE of 21.32% and excellent stability with PCE maintained 98% of its initial value after 1200 h for encapsulated device. Finally, a large-scale (1 cm^2) device with a maximum PCE of 19.01% was demonstrated with the optimized device architecture. This work provides a potential route for the controlled doping of inorganic CSLs to be integrated at a large scale, which is an important step towards commercialization.

Experimental Section

Materials.

Lead iodide (PbI_2, 99.9985%) was purchased from Alfa Aesar; lead bromide ($PbBr_2$, 99.999%) were purchased from Aladdin. Formamidinium iodide (FAI, ⩾99.5%) and methylammonium bromide (MABr, ⩾99.5%) were purchased from Xi'an Polymer Light Technology Corp. Dimethyl sulfoxide (DMSO, 99.9%), dehydrated solvents of chlorobenzene (CB, 99.9%) and N,Ndimethylformamide (DMF, 99.9%) was purchased from Sigma-Aldrich. Silver (Ag, 99.999%), titanium (Ti, 99.999%), cuprous oxide (Cu_2O, 99.9%), nickel oxide (NiO, 99.9%), niobium oxide (Nb_2O_5, 99.9%), and tungsten trioxide (WO_3, 99.9%) evaporation sources were purchased from ZhongNuo Advanced Material (Beijing) Technology. All the chemicals were used as received without further purification.

Perovskite Solar Cell Device Fabrication.

Deposition of Cu:NiO HTL: Pre-patterned ITO-coated glass substrates (Yaoke Optoelectronics, 10 Ω/sq) with sizes of 1.4 × 1.6 cm^2 were ultrasonically cleaned with a 1% Alconox detergent diluted in deionized water, deionized water, acetone, and isopropanol (IPA) in succession each for 15 min, and then dried under an air stream. Cu:NiO layer with a thickness of 30 nm was then deposited onto the ITO substrates by dual-source EB co-evaporation (Angstrom Engineering, AMOD) at a base pressure of $<5 \times 10^{-6}$ Torr. To achieve a Cu/Ni atomic ratio of approximately 3%, the deposition rates of NiO and Cu_2O were fixed at 2 and 0.07 Å s^{-1}, respectively. Post-annealing of the Cu:NiO thin films was carried out using a tube furnace in the air at 300 °C for 1 h.

***Deposition of perovskite films*:** $FA_{0.85}MA_{0.15}PbI_{2.55}Br_{0.45}$ perovskite solution was prepared by dissolving 1.02 M PbI_2, 0.18 M $PbBr_2$, 1.02 M FAI, and 0.18 M MABr in a mixed solvent of DMF: DSMO (4:1 v/v). The solution was stirred at 60 °C for 24 h in a nitrogen-filled glovebox and then

filtered through a 0.22-μm pore size PTFE syringe filter before use. Perovskite films were deposited by using a one-step spin-coating method in the nitrogen-filled glovebox. The perovskite solution (80 μL) was dropped onto the Cu:NiO-coated ITO substrate and spin-coated at a speed of 4000 rpm for 40 s and CB (100 μL) was dropped onto the spinning substrate at 20 s after the beginning of the spin-coating step. Then, the films were heated on a hotplate at 150 °C for 15 min in the nitrogen-filled glovebox.

Final PSC device assembly: W:Nb_2O_5 thin film with a thickness of ~60 nm was deposited onto the perovskite layer by dual-source EB co-evaporation at deposition rates of approximately 2 and 0.05 Å s^{-1} for Nb_2O_5 and WO_3, respectively. A long working distance (40 cm) between the sources and the substrate was used to minimize the possibility of the damage of perovskite surface by secondary electrons. Then, a Ti/Ag (10/100 nm) bi-layer electrode was deposited on top of the W:Nb_2O_5 ETL through a metal shadow mask by EB evaporation at a base pressure of ~5×10^{-6} Torr. The active areas of the PSCs were 0.155 and 1 cm^2, the unencapsulated and encapsulated devices were stored under dry conditions and characterized under ambient atmosphere.

Materials and Device Characterization.

SEM images of the samples were taken with ZEISS Crossbeam 340. XRD patterns were measured with Thermo Scientific ARL EQUINOX 1000 using Cu Kα source operated at 40 kV and 30 mA. HRTEM and STEM-EDS results were obtained using JEOL JEM2100F equipped with STEM unit and an EDS detector (Oxford Instruments).

For TEM observations, the cross section was glued by the epoxy resin and processed by means of a standard mechanical sample preparation process and finalized by Ar^+ ion-milling and polishing (PIPS II, GATAN) at grazing incidence (<5°). The acceleration voltage for HRTEM was 200 kV

and the spot size in STEM mode was 1 nm. XPS measurements were performed using a Kratos-Axis Supra system with a monochromatized Al Kα source. Charge neutralization was applied during measurement and the binding energy was calibrated using the hydrocarbon C 1s feature at 284.8 eV. UPS measurements were performed using a Thermo Scientific ESCA Lab 250Xi system with the HeI (21.22 eV) emission line. UV-Vis spectra of the samples were measured with SHIMADZU UV-1900. Steady-state PL and TRPL spectra were measured with Picoquant FluoTime 300 using a 510-nm picosecond laser with a maximum repetition rate of 40 MHz.

The photocurrent density voltage (J-V) curves were measured with a Keithley 2400 sourcemeter under reverse scan (open-circuit bias to short-circuit bias) using a class AAA solar simulator (SAN-EI ELECTRIC, XES-40S2) as the light source. The light intensity was calibrated to 1 Sun (100 mW/cm^2) using a certified reference cell (Konica Minolta AK-200). The spectral response was measured by an EQE measurement system (QEX10, PV Measurement) equipped with a monochromator, a lock-in amplifier, a Xe lamp, and a current-voltage amplifier. The EIS Nyquist plot was measured using a potentiostat (Bio-Logic SP-200) at a constant zero bias under 20-mV AC perturbation in the frequency range from 1 kHz to 1 MHz.

Acknowledgements

This work was supported by the National Natural Science Foundation of China (No. 21872019). A.M. and M.V. acknowledges the financial support from the Slovenian Research Agency (research core funding No. P2-0412 and project No. J2-2498).

Conflict of Interests

The authors declare no competing financial interests.

Supporting Information

Supporting Information is available from the Wiley Online Library or from the author

References

[1] D. Bogachuk, S. Zouhair, K. Wojciechowski, B. Yang, V. Babu, L. Wagner, B. Xu, J. Lim, S. Mastroianni, H. Pettersson, A. Hagfeldt, A. Hinsch, *Energy Environ. Sci.* **2020**, 13, 3880.

[2] Y. Xu, M. Wang, Y. Lei, Z. Ci, Z. Jin, *Adv. Energy Mater.* **2020**, 10, 2002558.

[3] F. Ali, C. Roldán- Carmona, M. Sohail, M. K. Nazeeruddin, *Adv. Energy Mater.* **2020**, 10, 2002989.

[4] J. Jeong, M. Kim, J. Seo, H. Lu, P. Ahlawat, A. Mishra, Y. Yang, M. A. Hope, F. T. Eickemeyer, M. Kim, Y. J. Yoon, I. W. Choi, B. P. Darwich, S. J. Choi, Y. Jo, J. H. Lee, B. Walker, S. M. Zakeeruddin, L. Emsley, U. Rothlisberger, A. Hagfeldt, D. S. Kim, M. Grätzel, J. Y. Kim, *Nature* **2021**, 592, 381.

[5] G. Kim, H. Min, K. S. Lee, D. Y. Lee, S. M. Yoon, S. I. Seok, *Science*, **2020**, 370, 108.

[6] J. Xi, I. Spanopoulos, K. Bang, J. Xu, H. Dong, Y. Yang, C. D. Malliakas, J. M. Hoffman, M. G. Kanatzidis, Z. Wu, *J. Am. Chem. Soc.* **2020**, 142, 19705

[7] X. Hu, C. Liu, Z. Zhang, X. F. Jiang, J. Garcia, C. Sheehan, L. Shui, S. Priya, G. Zhou, S. Zhang, K. Wang, *Adv Sci.* **2020**, 7, 2001285.

[8] S.-S. Rong, M. B. Faheem, Y.-B. Li, *J. Elec. Sci. Technol.* **2021**, 19, 100081.

[9] S. Seo, S. Shin, E. Kim, S. Jeong, N.-G. Park, H. Shin, *ACS Energy Lett.* **2021**, 6, 3332.

[10] S. Rong, Y. Xiao, J. Jiang, Q. Zeng, Y. Li, *J. Phys. Chem. C* **2020**, 124, 8992.

[11] M. B. Faheem, B. Khan, C. Feng, M. U. Farooq, F. Raziq, Y. Xiao, Y. Li, *ACS Energy Lett.* **2019**, 5, 290.

[12] Z. Wang, Q. Wei, X. Liu, L. Liu, X. Tang, J. Guo, S. Ren, G. Xing, D. Zhao, Y. Zheng, *Adv. Energy Mater.* **2020**, 31, 2008404.

[13] H. Lu, Y. Liu, P. Ahlawat, A. Mishra, W. R. Tress, F. T. Eickemeyer, Y. Yang, F. Fu, Z.

Wang, C. E. Avalos, B. I. Carlsen, A. Agarwalla, X. Zhang, X. Li, Y. Zhan, S. M. Zakeeruddin, L. Emsley, U. Rothlisberger, L. Zheng, A. Hagfeldt, M. Grätzel, *Science* **2020**, 370, 6512.

[14] J. Feng, Z. Yang, D. Yang, X. Ren, X. Zhu, Z. Jin, W. Zi, Q. Wei, S. Liu, *Nano Energy* **2017**, 36, 1.

[15] N. Arora, M. I. Dar, A. Hinderhofer, N. Pellet, F. Schreiber, S. M. Zakeeruddin, M. Grätzel, *Science* **2017**, 358, 768.

[16] J. W. Jung, C.-C. Chueh, A. K. Y. Jen, *Adv. Energy Mater.* **2015**, 27, 7874.

[17] C. Duan, M. Zhao, C. Zhao, Y. Wang, J. Li, W. Han, Q. Hu, L. Yao, H. Jian, F. Lu, T. Jiu, *Mater. Today Energy* **2018**, 9, 487.

[18] J. Jiang, Q. Wang, Z. Jin, X. Zhang, J. Lei, H. Bin, Z.-G. Zhang, Y. Li, S. F. Liu, *Adv. Energy Mater.* **2018**, 8, 1701757.

[19] J. Jiang, Z. Jin, J. Lei, Q. Wang, X. Zhang, J. Zhang, F. Gao, S. Liu, *J. Mater. Chem. A* **2017**, 5, 9514.

[20] W. Chen, Y. Wu, Y. Yue, J. Liu, W. Zhang, X. Yang, H. Chen, E. Bi, I. Ashraful, M. Grätzel, L. Han, *Science* **2015**, 350, 944.

[21] J. You, L. Meng, T. B. Song, T. F. Guo, Y. M. Yang, W. H. Chang, Z. Hong, H. Chen, H. Zhou, Q. Chen, Y. Liu, N. De Marco and Y. Yang, *Nat. Nanotechnol* **2016**, 11, 75.

[22] N. Arora, M. I. Dar, A. Hinderhofer, N. Pellet, F. Schreiber, S. M. Zakeeruddin, M. Grätzel, *Science* **2017**, 358, 768.

[23] S. Zhang, W. Chen, S. Wu, R. Chen, Y. Huang, Z. Yang, J. Li, L. Han, W. Chen, *J. Mater. Chem. A* **2019**, 7, 18603.

[24] X. Liu, J. Jiang, F. Wang, Y. Xiao, I. D. Sharp, Y. Li, *ACS Appl. Mater. Interfaces* **2019**, 11,

46894.

[25] X. Liu, Y. Xiao, Q. Zeng, J. Jiang, Y. Li, *J. Phys. Chem. Lett.* **2019**, 10, 6382.

[26] A. Bashir, J. H. Lew, S. Shukla, D. Gupta, T. Baikie, S. Chakraborty, R. Patidar, A. Bruno, S. Mhaisalkar, Z. Akhter, *Solar Energy* **2019**, 182, 225.

[27] M. Kim, C. W. Joo, J. H. Kim, W. Choi, J. Lee, D. Lee, H. Cho, H. Lee, S. Park, N. S. Cho, H. Cho, C.-W. Lee, D. Y. Jeon, B.-H. Kwon, *ACS Photonics* **2018**, 5, 3389.

[28] G. M. Arumugam, S. K. Karunakaran, C. Liu, C. Zhang, F. Guo, S. Wu, Y. Mai, *Nano Select* **2021**, 2, 1081.

[29] F. Ma, Y. Zhao, J. Li, X. Zhang, H. Gu, J. You, *J. Energy Chem.* **2021**, 52, 393.

[30] W. Chen, Y. Wu, J. Fan, A. B. Djurišić, F. Liu, H. W. Tam, A. Ng, C. Surya, W. K. Chan, D. Wang, Z.-B. He, *Adv. Energy Mater.* **2018**, 8, 1703519.

[31] Y.-H. Li, X. Lu, R. Wang, Y.-Y. Ma, S. Duhm, M.-K. Fung, *J. Mater. Chem. C* **2017**, 5, 11751.

[32] W. Chen, Y. Wu, Y. Yue, J. Liu, W. Zhang, X. Yang, H. Chen, E. Bi, I. Ashraful, M. Grätzel, L. Han, *Science* **2015**, 350, 944.

[33] A. Esteves, L. C. Oliveira, T. C. Ramalho, M. Goncalves, A. S. Anastacio, H. W. Carvalho, *Catal. Commun.* **2008**, 10, 330.

[34] Y. Chen, Z. Pu, Y. Liu, Y. Shen, S. Liu, D. Liu, Y. Li, *J. Power Sources* **2021**, 515, 230601.

[35] E. Pehlivan, F. Z. Tepehan, G. G. Tepehan, *Solid State Ionics* **2003**, 165, 105.

[36] S. Wu, R. Chen, S. Zhang, B. H. Babu, Y. Yue, H. Zhu, Z. Yang, C. Chen, W. Chen, Y. Huang, S. Fang, T. Liu, L. Han, W. Chen, *Nat. Commun.* **2019**, 10, 1161.

[37] H.-L. Chen, Y.-S. Yang, *Thin Solid Films*. **2008**, 516, 5590.

[38] D. Adler, J. Feinleib, *Phys. Rev. B* **1970**, 2, 3112.

[39] P. Li, Y. Zhang, C. Liang, G. Xing, X. Liu, F. Li, X. Liu, X. Hu, G. Shao, Y. Song, *Adv. Energy Mater.* **2018**, 30, 1805323.

[40] G. Xing, N. Mathews, S. Sun, S. S. Lim, Y. M. Lam, M. Grätzel, S. Mhaisalkar, T. C. Sum, *Science* **2013**, 342, 344.

[41] J. Jiang, X. Lang, Q. Zeng, M. B. Faheem, H. Zhao, Y. Li, *J. Mater. Chem. A* **2021**, 9, 13220.

[42] E. Bi, W. Tang, H. Chen, Y. Wang, J. Barbaud, T. Wu, W. Kong, P. Tu, H. Zhu, X. Zeng, J. He, S.-i. Kan, X. Yang, M. Grätzel, L. Han, *Joule* **2019**, 3, 2748.

[43] J. Jiang, Z. Jin, F. Gao, J. Sun, Q. Wang, S. F. Liu, *Adv. Sci.* **2018**, 5, 1800474.

[44] Z. Jin, M. Yuan, H. Li, H. Yang, Q. Zhou, H. Liu, X. Lan, M. Liu, J. Wang, E. H. Sargent, Y. Li, *Adv. Funct. Mater.* **2016**, 26, 5284.

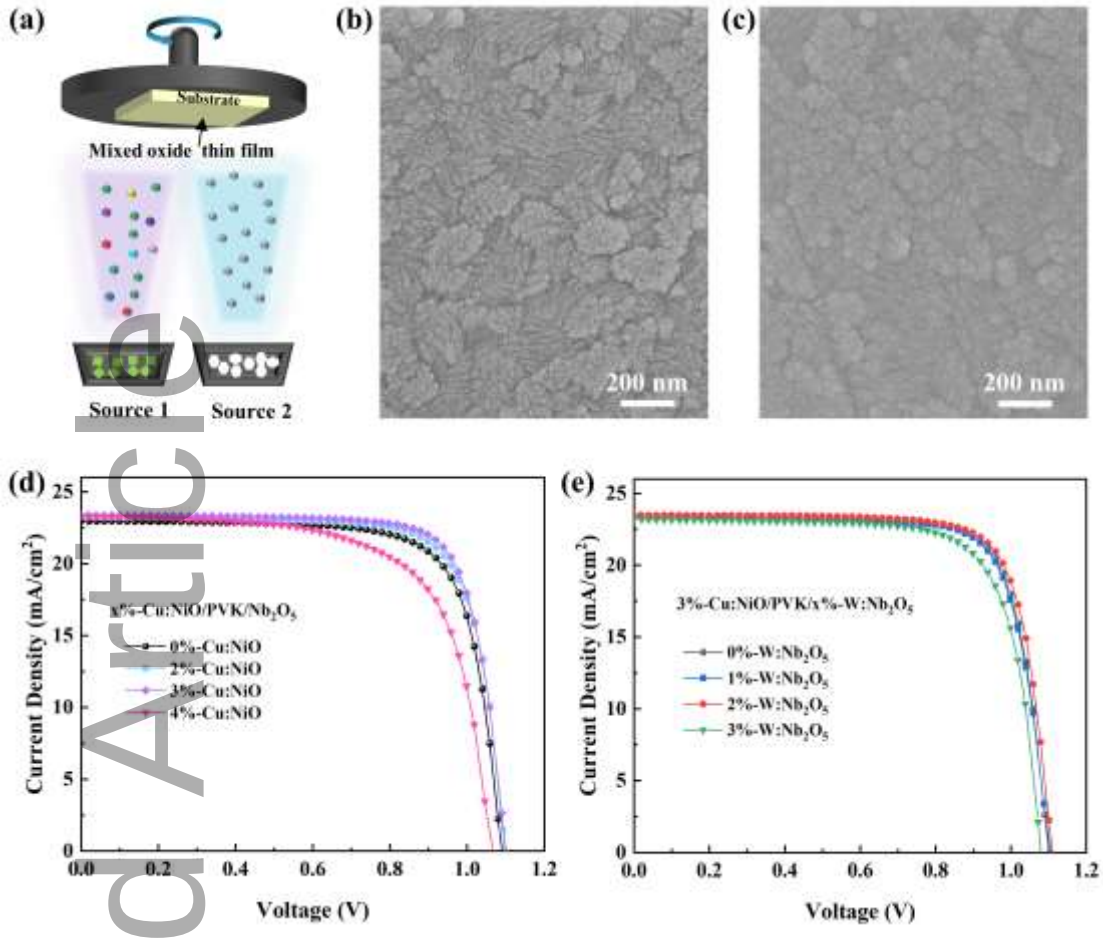

Figure 1. (a) Schematic drawing for the dual-source EB co-evaporation of doped inorganic CSLs. (b) SEM image of a 3%-Cu:NiO film on ITO substrate. (c) SEM image of a 2%-W:Nb_2O_5 film on ITO substrate. (d) *J*-V curves of PSCs with different Cu doping concentrations in NiO HTL. (e) *J*-V curves of 3%-Cu:NiO HTL based PSCs with different W doping concentrations in Nb_2O_5 ETL.

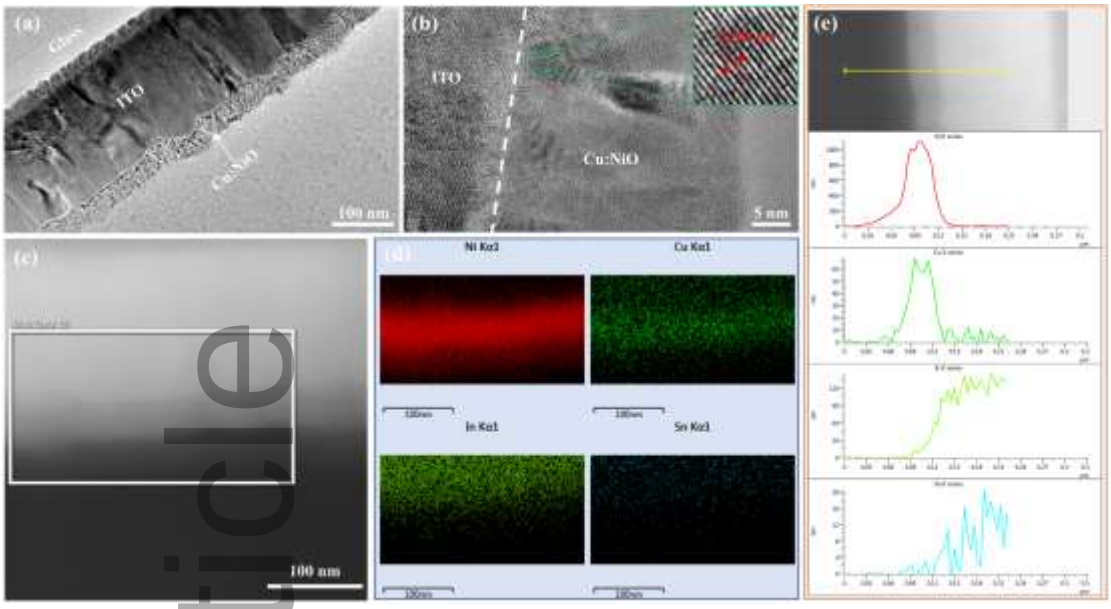

Figure 2. (a-b) HRTEM images of Cu:NiO thin film deposited on ITO substrate. Inset in (b) shows the lattice fringes of Cu:NiO with a d-spacing of 0.245 nm. (c) STEM image of the Cu:NiO thin film on ITO substrate. White square indicates the area for EDS mapping. (d) STEM-EDS mapping for Ni, Cu, In, and Sn elements. (e) STEM-EDS line scans for Ni, Cu, In, and Sn elements.

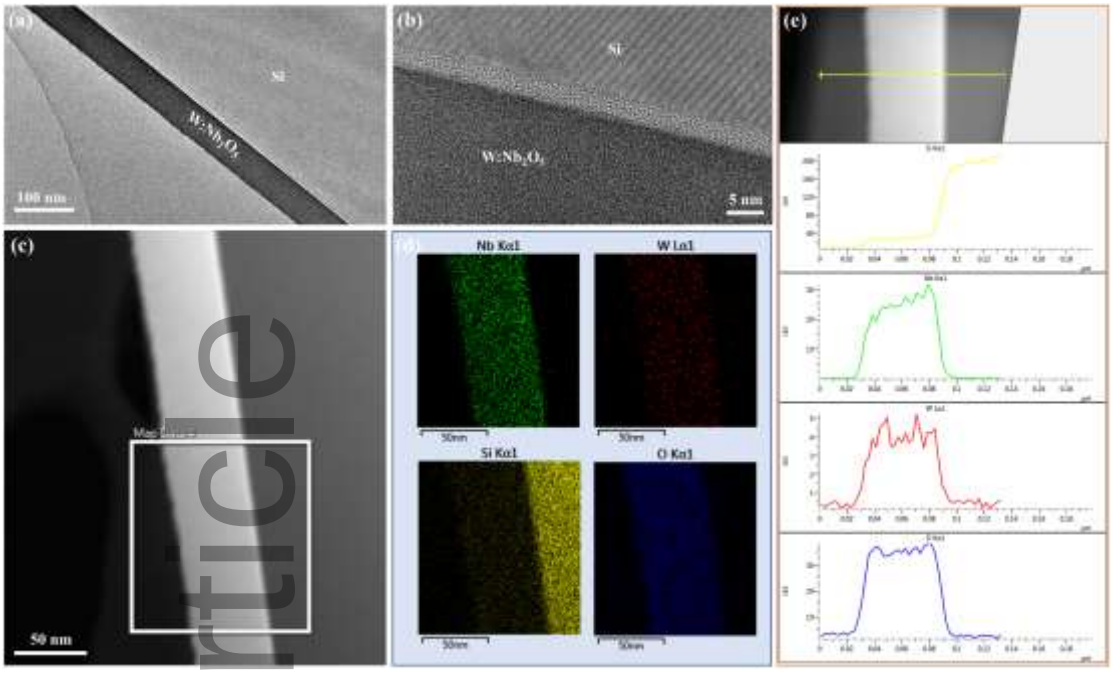

Figure 3. (a-b) HRTEM images of $W:Nb_2O_5$ thin film deposited on Si substrate. (c) STEM image of the $W:Nb_2O_5$ thin film on Si substrate. White square indicates the area for EDS mapping. (d) STEM-EDS mapping for Nb, W, Si, and O elements. (e) STEM-EDS line scans for Nb, W, Si, and O elements.

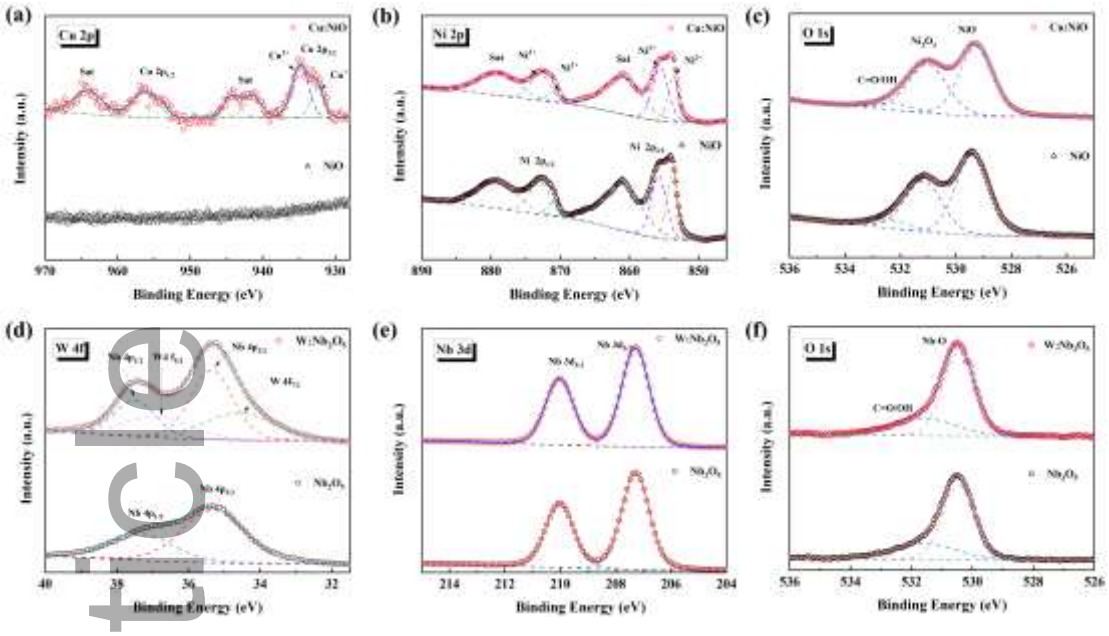

Figure 4. (a-c) XPS core-level spectra of Cu 2p (a), Ni 2p (b), and O 1s (c) for NiO and Cu:NiO films. (d-f) XPS core-level spectra of W 4f overlapped with Nb 4p (d) , Nb 3d (e), and O 1s (f) for Nb_2O_5 and W:Nb_2O_5 films.

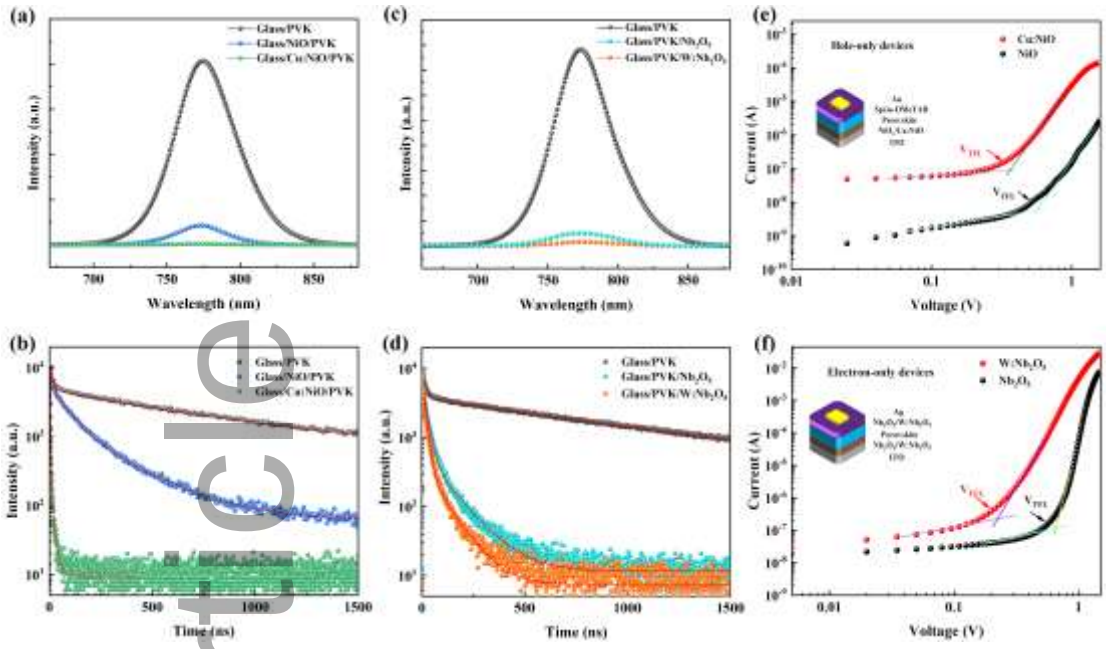

Figure 5. (a-b) Steady-state PL spectra (a) and TRPL decay curves (b) of perovskite films deposited on glass substrates and on NiO- or Cu:NiO-coated glass substrates. (c-d) Steady-state PL spectra (c) and TRPL decay curves (d) of perovskite films deposited on glass substrates and with/without Nb_2O_5/W: Nb_2O_5 ETLs. (e-f) Dark I-V plots of the hole-only (e) and electron-only (f) devices. The schematic structures of the hole-only and electron-only devices are depicted in the insets.

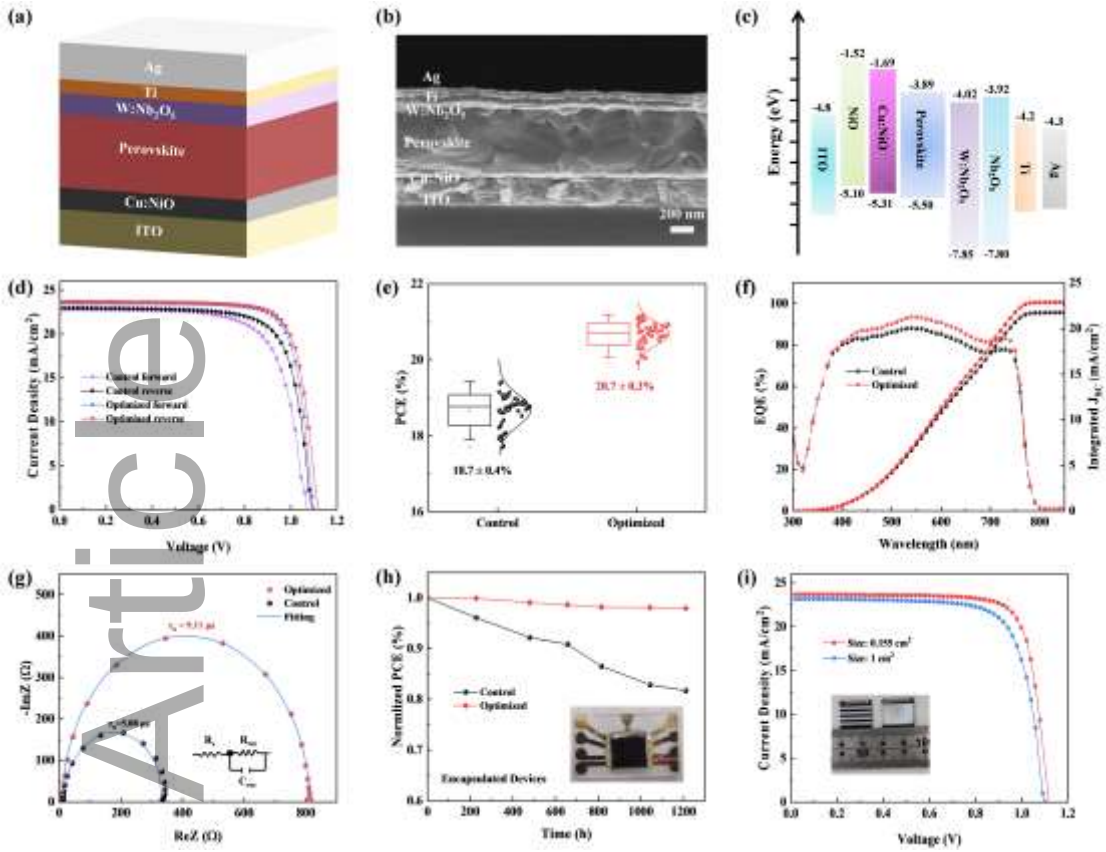

Figure 6. (a) Device architecture of the optimized inverted planar PSC. (b) Cross-sectional SEM image of the optimized PSC. (c) Energy level diagram of the functional layers of the control and optimized PSCs. (d) *J*-V curves measured under reverse and forward scan directions for the control and optimized PSCs. (e) Statistical distribution of PCEs measured under reverse scan for 50 individual control and optimized devices. (f) EQE spectra and integrated J_{SC} curves of the control and optimized devices. (g) Nyquist plots of the control and optimized devices. (h) Stability test of encapsulated (inset) control and optimized devices. (i) *J*-V curves measured under reverse scan for the PSCs with effective areas of 0.155 and 1 cm^2.

Table 1. *J*-V parameters of ITO/x%-Cu:NiO/perovskite/Nb_2O_5/Ag PSCs with different Cu-doping concentrations.

Cu:NiO (%)	V_{OC} (V)	J_{SC} (mA/cm^2)	FF (%)	PCE (%)
0	1.091	22.96	75.9	19.02
2	1.095	23.28	76.4	19.48
3	1.101	23.37	77.5	19.94
4	1.045	23.26	69.1	16.80

Table 2. *J*-V parameters of ITO/3%-Cu:NiO/perovskite/x%-W:Nb_2O_5/Ag PSCs with different W-doping concentrations.

W:Nb_2O_5 (%)	V_{OC} (V)	J_{SC} (mA/cm^2)	FF (%)	PCE (%)
0	1.101	23.37	77.5	19.94
1	1.106	23.34	77.8	20.08
2	1.109	23.48	78.6	20.47
3	1.079	23.16	75.5	18.86

Table 3. *J*-V parameters of the control and optimized devices with different scan directions.

Device	Scanning mode	J_{SC} (mA/cm^2)	V_{OC} (V)	FF (%)	PCE (%)
Control	Reverse	22.96	1.091	75.9	19.02
	Forward	22.84	1.071	71.5	17.49
Optimized	Reverse	23.68	1.121	80.3	21.32
	Forward	23.57	1.097	79.6	20.60

Table 4. The key *J*-V parameters of the optimized devices with different active areas.

Active area (cm^2)	V_{OC} (V)	J_{SC} (mA/cm^2)	FF (%)	PCE (%)
0.155	1.121	23.68	80.3	21.32
1	1.096	23.16	74.9	19.01

TOC

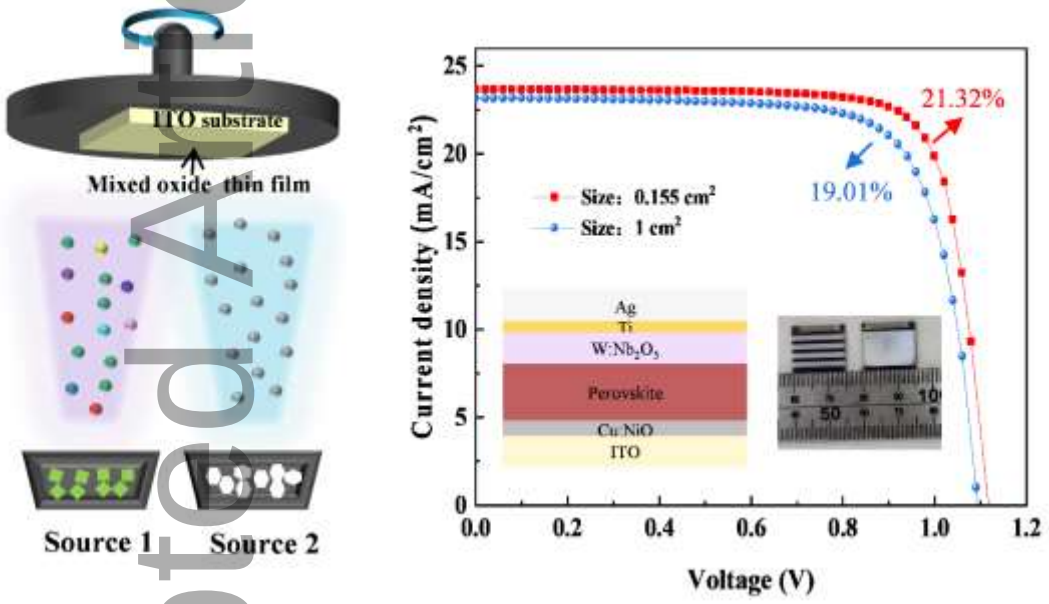

A dual-source electron-beam co-evaporation method is employed for the controlled deposition of copper-doped nickel oxide and tungsten-doped niobium oxide as hole and electron transport layers, respectively. Perovskite solar cells based on these inorganic carrier selective layers achieve power conversion efficiencies of 21.32% for a 0.155-cm^2 device and 19.01% for a 1-cm^2 device.